www.sensorsportal.com

Sensors & Transducers

Published by IFSA Publishing, S. L., 2026
http://www.sensorsportal.com

A Multi-Objective LQR-Based Motion Cueing Framework for Redundant Ski Simulators with Human Perception Integration

[1, *] Taha HOUDA, [2] Lotfi BEJI and Ali AMOURI
[1] Computer Engineering department, Prince Mohammad Bin Fahd University, Alkhobar, Saudi Arabia
[2] ISAT Nevers, Université de Bourgogne (UBE), France
[3] IBISC Laboratory, University of Paris-Saclay, Évry-Courcouronnes, France
Tel.: + 966 506468532
E-mail: thouda@pmu.edu.sa, lotfi.beji@u-bourgogne.fr, ali.amouri@univ-evry.fr

Received: 31 March 2026 /Revised: 4 May 2026 /Accepted: 20 May 2026 /Published:29 June 2026

Abstract: To facilitate the integration of people with disabilities into sports domains using simulators, particularly in the field of skiing, this article proposes a solution to the Motion Cueing Algorithm (MCA) parameter optimization problem under some human-platform interactions and environment constraints, distinguished here as a multi-objective problem. The considered simulator is redundant with respect to skier's motions and to generate high-fidelity movements, the Linear-Quadratic Regulator (LQR) method is employed to minimize the human perceptual error between the real and simulated skier environments. Both the vestibular model and the redundant simulator constraints are considered in MCA parameter optimization. Linear time-invariant representations are detailed and the appropriate optimal control parameters are solved. The implemented skier scenarios demonstrate the improvement in human sensation and the efficiency of the proposed redundancy resolution method.

Keywords: Optimal control, Human sensation, Hybrid robot, Motion cueing algorithm, Redundancy resolution.

1. Introduction

3D interactions in mixed reality environments and their integration into industry have recently experienced significant growth [1, 2]. A crucial question for the design and validation of a modern simulator is how to combine mechanical systems and virtual tools [3]. The best-known examples are driving simulators [4] and flight simulators [5], which have contributed much knowledge to the automotive and aerospace industries. They can help study the effects of implementing active safety technologies and driver assistance, and explore human factors such as driver response to road conditions and aging [6].

Handiskiing [7, 8], which combines the words Disability and Alpine Skiing, refers to the adaptation of alpine skiing to people with disabilities. It is a new sport that has attracted a lot of interest from enthusiasts who enjoy practicing it every year. However, there are many constraints on ski training, especially for people with disabilities. There are environmental dependencies, as skiing requires a good amount of snow and slopes, which limits the sport to adapted resorts. For this reason, ski simulators are becoming increasingly popular in the ski sports industry due to their ability to replicate real snow conditions and provide users with an immersive experience. They use advanced technologies to reproduce sliding movements, gravity and snow vibrations, such as Motion Cueing Algorithm (MCA) [9, 10]. Ski simulators can also be coupled with virtual reality to increase immersion and human sensation. A motion simulator proves to be an effective tool that allows training of people with various joint diseases while maintaining a clinical safety environment [11]. In addition, these simulators provide psychological, muscular and social benefits for people with severe disabilities [12]. A Motion-Cueing Algorithm (MCA), also known as a washout filter algorithm, is the strategy that controls how motion cues are generated while keeping the motion of the platform within its physical limits [10]. The main goal is to provide realistic motion cues to the pilot or seated skier in the simulator while keeping the motion platform within its physical limits.

In [13, 14], several washout algorithms have been proposed. Many researchers have modified and improved these algorithms in recent years [15, 16]. They can mainly be divided into classical, adaptive and optimal cueing algorithms. The classical approach consists of defining fixed coefficients in the worst-case maneuvers, which degrades the quality of motion perception in moderate maneuvers. Moreover, it can generate wrong cues due to the filter characteristics and lead to wrong motion signals. The main drawback of the classical washout filter is that it does not take human perception into account. The adaptive approach was implemented by Reid and Nahon [17]. It eliminates this shortcoming by adaptively modifying the coefficients and providing better motion sensation. Several motion cueing approaches have been proposed in recent years. Qazani et al. [18] introduced a fuzzy logic-based adaptive motion cueing algorithm to improve simulator performance under varying operating conditions. However, such approaches are mainly heuristic and do not explicitly incorporate a detailed mathematical model of human motion perception. Nahavandi [19] emphasized the importance of human-centric design in modern engineering systems, highlighting the need to integrate human perception into control strategies. In this direction, Gharib et al. [20] proposed an evolutionary optimal washout filter based on a genetic algorithm, aiming to optimize motion cueing performance through advanced optimization techniques. This optimal washout filter algorithm was based on human motion perception and considered a mathematical model of the human vestibular system [21].

The optimal algorithm, which uses LQR-based control techniques, attempts to provide higher-order filters prior to real-time application to minimize the error of motion sensing rather than motion states while maintaining the physical limits of the simulator. To the best of our knowledge, all existing ski simulators use only a 2-DoF mechatronic system, which is not sufficient to reproduce all the skier's movements. In general, most simulation platforms use only one hexapod platform. As a result, fewer research studies have addressed MCA for hybrid platforms. A so-called XY table is a significant improvement over the conventional simulators, which are able to perform larger translational motion in the longitudinal and transverse directions. The hexapod (6-DoF) is mounted above a table (2-DoF), giving a total of eight degrees-of-freedom (8-DoF). Thus, the human operator is exposed to both motions. Therefore, we propose a VR based high degree-of-freedom indoor ski training system, an 8-DoF simulator. Using this training system, we replay the movement of an expert skier recorded on a virtual slope and can reproduce this movement in the simulator as closely as possible [22].

In recent years, an increasing number of kinematically redundant robots have been used in various fields of robotics [23, 24]. This may be due to the focus on increasingly constrained environments where the conventional six degrees of freedom (6-DOF) may prove insufficient for obstacle avoidance and singularity [25, 26]. Kinematic redundancy occurs when a manipulator has more degrees of freedom than are required to perform a particular task. Thus, it is widely recognized that a seven-joint robotic arm following an end-effector motion trajectory requiring six degrees of freedom is generally considered an example of an inherently redundant manipulator. This means that a particular position and orientation of the end effector determines an entire solution space, rather than a single solution. To obtain a particular configuration (or joint velocities/moments), a redundancy resolution method should select the element with the "best fit" in the solution space. The simplest method uses the pseudo-inverse of the Jacobian matrix. This guarantees a least-squares reconstruction of the desired end-effector velocity. A drawback of this method is that singularity avoidance cannot be guaranteed despite local minimization of joint velocities [27].

This journal article extends our previous conference work [28] with several significant contributions. First, a complete and explicit state-space formulation of the human vestibular system is provided, including both otolith and semicircular canal dynamics, whereas the conference version presented a more limited formulation. Second, a simplified and computationally efficient linear time-invariant (LTI) representation is introduced to facilitate real-time implementation of the motion cueing algorithm. Third, perceptual thresholds of the human vestibular system are explicitly incorporated into the MCA design, improving the realism of the generated motion cues. Fourth, the LQR-based formulation is extended with a fully specified cost function, explicit weighting matrices, and a reproducible numerical setup. Fifth, the redundancy resolution strategy is further developed and formalized, including a clear algorithmic implementation for motion distribution between the hexapod and the XY table. Finally, a quantitative performance evaluation is introduced through a well-defined performance indicator (PI), allowing comparison with classical, adaptive, and optimization-based approaches. These extensions significantly enhance the rigor, reproducibility, and practical applicability of the proposed method compared to the conference version.

In this article, we describe the model of human motion perception in Section 2. Then, in Section 3, we explain the optimal MCA control based on the LQR theory. In Section 4, we develop a redundancy solution method that makes the simulator nonredundant with respect to the task by finding the appropriate motion distribution of the XY table and the hexapod. Finally, in Section 5, we draw a conclusion and give an outlook of the work.

2. Human Motion Perception System

The vestibular system illustrated in Fig. 1 is a set of organs located in the inner ear and responsible for detecting inertial movements, whether translation or rotation. There are two subsystems: the otolith organs and the semicircular canals, responsible for the detection of translation and rotation, respectively. A certain threshold of detection must be crossed to feel a movement.

According to [29], the specific stimulus of the otolith organs is the shear force between the two layers of the otolith membrane. The deformation of the gelatinous layer will induce the bending of the hair cells. The operation that transforms the biomechanical signal (bending of the hair cells) into nervous impulses (electrical activity of the hair cells) is the transduction mechanism [30]. When the hair cells tilt towards the kinocil, this causes depolarization. The frequency of the action potentials (nerve impulses noted Ni and measured in ips: impulse per second) is sent to the brain. When the hair cells tilt in the opposite direction, the sensory cells are hyperpolarized and the production of action potentials decreases. The variations in polarization (excitation and inhibition) lead to a variation in the frequencies of the action potentials of the afferent fibers.

Each semi-circular canal has a swollen base (bulb) that contains sensory cells and a cup (elastic gelatinous membrane denser than the endolymph). The bulbs also have a receptor area (sensory epithelium) called the ampullary ridge, similar to the macula of otoliths. As with otoliths, this area is involved in the transformation of the rotational movement of the head into a neuronal signal. The cupula is a gelatinous membrane, attached to the base of the ampullary ridge and the top of the bulb. The crista ampullaris or crista ampullaris (thick, rounded area) contains the hair cells responsible for neural transmission. When a rotational movement of the head occurs in the plane of one of the canals, the endolymph undergoes an inertial force with respect to the labyrinth and deforms the cupula. This deformation of the cup causes the hair cells to bend in the direction opposite to the movement (inertia). The fluid then continues to rotate in the canal at the same rate as the rotation. However, when the rotation continues at constant speed, the cup returns to its equilibrium position (non-linear phenomenon of saturation in neutral position and energy accumulation). Then, at the end of the rotation, the endolymph-cup system reacts in the opposite direction (energy discharge) of the one of the rotations which was completed. Finally, the cup returns to its initial position.

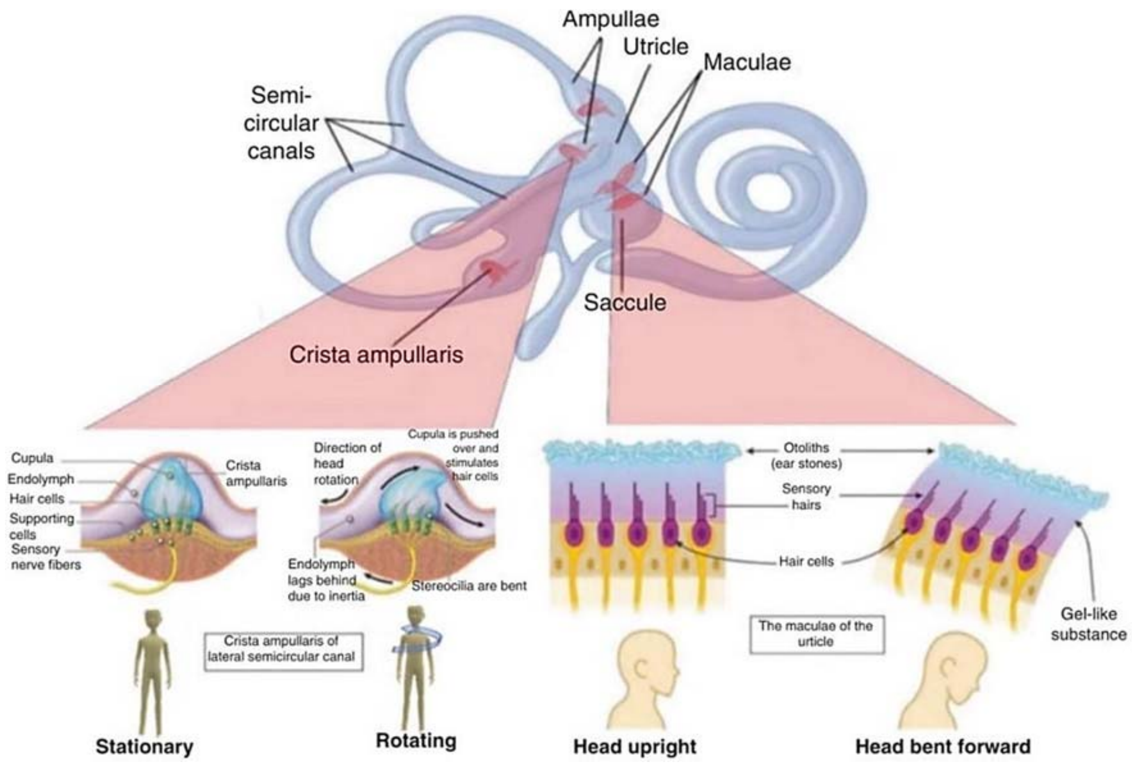

Fig. 1. Motion transduction, Rest vs otoliths (a) and semicircular canals (b) subjected to linear and rotational motion, respectively [29].

The proposed MCA must consider the human sensation model. The development of a mathematical model of the vestibular system is therefore crucial.

In the literature, the otolithic subsystem dynamics are modeled as a mass-spring-damper absorber [31] and [32]. This dynamic is modeled by the following second-order filter:

$$\frac{\hat{F}(s)}{F(s)} = K_{oto}\frac{\tau_L s + 1}{(1+\tau_1 s)(1+\tau_2 s)}, \tag{1}$$

where τ_1, τ_2 , and τ_L are long time, short time, and lead term constants, respectively, and s is the Laplace operator. $\hat{F}$ is the felt specific force and F is the stimulating specific force at the head level. Recall that the specific force is the difference between the linear acceleration and the gravity vector since, at rest, the otolithic organs undergo vertical gravity acceleration.

However, the dynamics of the semicircular canal subsystem are modeled as an overdamped pendulum [33–35]. This dynamic can be modeled by the following second-order low-pass filter:

$$\frac{\hat{\Omega}(s)}{\Omega(s)} = K_{scc}\frac{\tau_1\tau_a s^2(1+\tau_L s)}{(1+\tau_a s)(1+\tau_1 s)(1+\tau_2 s)}, \tag{2}$$

where $\hat{\Omega}$ is the felt angular velocity, Ω is the head angular velocity and τ_1, τ_2 , τ_L and τ_a are long time, short time, lead term, and adaptation operator constants, respectively. In the context of motion restitution using a motion simulator, there are three modes. The first mode is the longitudinal mode, also called surge/pitch mode which consists of a translation along the x-axis and a rotation θ_y around the y-axis. The second mode is the transverse mode where the translation is along the y-axis and the rotation θ_x is around x-axis and finally the third mode is the vertical mode which consists only of a translation along the z-axis. These modes are decoupled at the level of human sensations and, consequently, at the level of the vestibular system [28]. Therefore, the development of each mode occurs separately and in a similar way. Therefore, in this article, we present and develop below the algorithm of the longitudinal mode only (x, θ_y).

We develop the state space representation of the vestibular system constituting the otolith subsystem and the semicircular canal subsystems. The otolith's dynamic (1) in the longitudinal mode can be rewritten as:

$$\frac{\hat{F}_x(s)}{F_x(s)} = \overline{K}_{oto}\frac{(s+\frac{1}{\tau_L})}{(s+\frac{1}{\tau_1})(s+\frac{1}{\tau_2})}, \tag{3}$$

where $\underline{K}_{oto} = K_{oto}\frac{\tau_L}{\tau_1\,\tau_2}$ is defined as the static sensitivity.

Let us define the input as:

$$U(s) = \left(U_1(s)U_2(s)\right)^T\left(s\Theta y(s)s^2X(s)\right)^T,$$

where $(\quad)^T$ denotes the transpose. The specific force in the longitudinal mode is expressed by

$$F_x(s) = s^2X(s) + g\Theta y(s)$$

Therefore, $F_x(s) = U_2(s) + \left(g\,\frac{1}{s}\right)U_1(s)$.

Substituting $F_x(s)$ into (3) and introduce the Laplace inverse transformation leads to:

$$\begin{aligned}\ddot{\hat{f}}_x + \left(\frac{\tau_1+\tau_2}{\tau_1\tau_2}\right)\dot{\hat{f}}_x + \frac{\hat{f}_x}{\tau_1\tau_2} = \\ = \overline{K}_{oto}\left(gu_1 + \frac{g}{\tau_L}\int u_1 dt + \dot{u}_2 + \frac{u_2}{\tau_L}\right),\end{aligned} \tag{4}$$

where $f_x(t) = u_2(t) + g\int u_1(t)\,dt$ and $u(t) = \left(\dot{\theta}_y(t)\ddot{x}(t)\right)^T$.

We retain the model of the head movement (u_1, u_2) and the human sensation at the otolith level:

$$\begin{aligned}\ddot{\hat{f}}_x + \lambda_1\dot{\hat{f}}_x + \lambda_2\hat{f}_x = \lambda_3\dot{u}_1 + \lambda_4 u_1 + \\ +\lambda_5\int u_1 dt + \lambda_6\dot{u}_2 + \lambda_7 u_2),\end{aligned} \tag{5}$$

(Sensation dynamics = Input dynamics),

where

$$\begin{aligned}\lambda_1 = \frac{\tau_1+\tau_2}{\tau_1\tau_2}, \lambda_2 = \frac{1}{\tau_1\tau_2},\\ \lambda_3 = 0, \lambda_4 = \overline{K}_{oto}\,g,\\ \lambda_5 = \overline{K}_{oto}\frac{g}{\tau_L}, \lambda_6 = \overline{K}_{oto}, \lambda_7 = \frac{\overline{K}_{oto}}{\tau_L}\end{aligned} \tag{6}$$

Let us consider the state vector $x_{oto} = (x_{oto1}x_{oto2}x_{oto3})^T$ as follows:

$$\begin{aligned}x_{oto1} &= \hat{f}_x\,,\\ x_{oto2} &= \dot{x}_{oto1} - \lambda_3 u_1 - \lambda_6 u_2,\\ x_{oto3} &= \lambda_5\int u_1 dt\end{aligned} \tag{7}$$

By taking the derivative state $\dot{x}_{oto1}$, we get the following LTI (Linear Time Invariant) model:

$$\begin{aligned}\dot{x}_{oto} &= A_{oto}\,x_{oto} + B_{oto}\,u,\\ y_{oto} &= C_{oto}\,x_{oto} + D_{oto}\,u\end{aligned} \tag{8}$$

where $x_{oto} \in \mathbb{R}^3$, $y_{oto} \in \mathbb{R}$ and $u = (u_1u_2)^T \in \mathbb{R}^2$, are the otoliths states, output and the vestibular system input, respectively. The constant matrices are given as:

$$\begin{aligned}A_{oto} = \begin{pmatrix}0 & 1 & 0\\ -\lambda_2 & -\lambda_1 & 1\\ 0 & 0 & 0\end{pmatrix}; C_{oto} = (1 \quad 0 \quad 0),\\ B_{oto} = \begin{pmatrix}\lambda_3 & \lambda_6\\ \lambda_4-\lambda_1\lambda_3 & \lambda_7-\lambda_1\lambda_6\\ \lambda_5 & 0\end{pmatrix}; D_{oto} = (0 \quad 0)\end{aligned} \tag{9}$$

The semicircular subsystem dynamic (2) can be rewritten as:

$$\frac{\hat{\Omega}(s)}{\Omega(s)} = \frac{\beta_4 s^3+\beta_3 s^2}{s^3+\beta_2 s^2+\beta_1 s+\beta_0}, \tag{10}$$

where

$$\beta_0 = \frac{1}{\tau_a\tau_1\tau_2},\ \beta_1 = \frac{\tau_a+\tau_1+\tau_2}{\tau_a\tau_1\tau_2},$$
$$\beta_2 = \frac{\tau_1\tau_2+\tau_a(\tau_1+\tau_2)}{\tau_a\tau_1\tau_2},\ \beta_3 = \frac{K_s cc}{\tau_2}, \quad (11)$$
$$\beta_4 = \frac{K_{scc}\tau_L}{\tau_2}$$

Let us take the semicircular states $x_{scc} = (x_{scc1}\, x_{scc2}\, x_{scc3})^T \in \mathbb{R}^3$ follows:

$$\begin{aligned} x_{scc1} &= \widehat{\omega}, \\ x_{scc2} &= \dot{x_{scc1}} + \beta_2 x_{scc1} - (\beta_3 - \beta_2\beta_4)u_1, \\ x_{scc3} &= \dot{x_{scc2}} + \beta_1 \dot{x_{scc1}} + \beta_1\beta_4 u_1 \end{aligned} \quad (12)$$

By taking the derivative state $\dot{x_{scc}}$, we can get the following semicircular model in LTI form as:

$$\begin{aligned} \dot{x_{scc}} &= A_{scc}x_{scc} + B_{scc}u, \\ y_{scc} &= C_{scc}x_{scc} + D_{scc}u \end{aligned} \quad (13)$$

where $y_{scc} = \widehat{\omega_{scc}}$ the felt rotation speed and its canonical observer matrices are:

$$\begin{aligned} A_{scc} &= \begin{pmatrix} -\beta_2 & 1 & 0 \\ -\beta_1 & 0 & 1 \\ -\beta_0 & 0 & 0 \end{pmatrix}; C_{scc} = (1 \quad 0 \quad 0), \\ B_{scc} &= \begin{pmatrix} \beta_3 - \beta_2\beta_4 & 0 \\ -\beta_1\beta_4 & 0 \\ -\beta_0\beta_4 & 0 \end{pmatrix}; D_{scc} = (\beta_4 \quad 0) \end{aligned} \quad (14)$$

The state space representation of the human vestibular system (v), which consists of both semicircular model and otolith subsystems, can be presented as follows:

$$\begin{aligned} \dot{x_v} &= A_v x_v + B_v u, \\ y_v &= C_v x_v + D_v u, \end{aligned} \quad (15)$$

where $x_v = (x_{scc}\, x_{oto})^T \in \mathbb{R}^6$contains the vestibular states, $y_v = (y_{scc}\, y_{oto})^T \in \mathbb{R}^2$ is the felt output representation, and $A_v \in \mathbb{R}^{6\times6}$, $B_v \in \mathbb{R}^{6\times2}$, $C_v \in \mathbb{R}^{2\times6}$, and $D_v \in \mathbb{R}^{2\times2}$ are:

$$\begin{aligned} A_v &= \begin{pmatrix} A_{scc} & 0_{(3\times3)} \\ 0_{(3\times3)} & A_{oto} \end{pmatrix}, \\ C_v &= \begin{pmatrix} C_{scc} & 0_{(3\times3)} \\ 0_{(3\times3)} & C_{oto} \end{pmatrix}, \\ B_v &= \begin{pmatrix} B_{scc} \\ B_{oto} \end{pmatrix}; D_v = \begin{pmatrix} D_{scc} \\ D_{oto} \end{pmatrix} \end{aligned} \quad (16)$$

The mathematical modeling of the vestibular system is illustrated in Fig. 2, which presents the conventional representation combining both the otolith and semicircular canal dynamics. This model reflects the detailed physiological behavior of human motion perception and serves as the basis for motion cueing design.

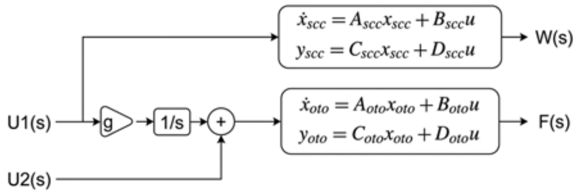

Fig. 2. The existing mathematical model of the vestibular system.

To facilitate the control design and integration within the optimal framework, a simplified state-space representation is proposed, as shown in Fig. 3. This representation reformulates the vestibular dynamics into a compact linear time-invariant (LTI) structure, enabling efficient implementation within the LQR-based optimization process. The proposed model preserves the essential perceptual dynamics while significantly reducing the computational complexity, making it suitable for real-time motion cueing applications.

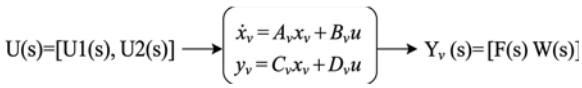

Fig. 3. The proposed simplified state space representation of the vestibular system.

The human vestibular system is characterized by perceptual thresholds below which motion stimuli are not consciously perceived. These thresholds play a crucial role in motion cueing design, as they define the limits within which discrepancies between real and simulated motion can remain imperceptible to the user. In particular, the otolith organs exhibit a detection threshold for linear acceleration typically in the range of 0.01 to 0.05 g (≈ 0.1–0.5 m/s²), while the semicircular canals have angular velocity detection thresholds on the order of 0.1 to 0.5 deg/s, with angular acceleration thresholds around 0.5 to 2 deg/s². When the generated motion signals remain below these thresholds, the human operator does not detect inconsistencies, allowing the simulator to operate within constrained physical limits while maintaining perceptual realism. Therefore, these thresholds are explicitly considered in the MCA design to ensure that the generated motion cues do not exceed human perception limits during washout and tilt coordination processes, thereby preserving motion fidelity and avoiding false or misleading sensations.

In addition to human perception constraints, the physical behavior of the motion platform must also be considered. The XY-6 DoF simulator is a nonlinear and coupled robotic system whose dynamics can be described using the standard rigid-body formulation:

$$\Gamma = M(q)\,\ddot{q} + H(q,\dot{q}),$$

where $\Gamma \in \mathbb{R}^8$ denotes the actuator torque vector, $q \in \mathbb{R}^8$ represents the generalized coordinates, $M(q)$ is the inertia matrix, and $H(q, \dot{q})$ includes Coriolis and gravitational effects. This model has been previously developed and validated in our earlier work [15]. The integration of both perceptual thresholds and system dynamics enables a unified framework for motion cueing optimization, which is presented in the following section.

3. MCA Multi-Objective Resolution

Simulator performance is measured by how well the following three objective functions are satisfied:

1. obj1: approximate the specific forces sensed by the human performing an application in the real world to the human performing the same application on a simulator;
2. obj2: respect the simulator's displacement, speed and acceleration limits;
3. obj3: do not exceed certain otoliths and semicircular canals thresholds in the washout and tilting operations.

Let us call the known human movement in real application the "predefined motion - pd" and the human movement on the simulator the "simulated motion - s". Thus, we can define the sensitive error $y_{v,e} \in \mathbb{R}^2$ as the difference in human perception between real $y_{v,pd}$ and simulated $y_{v,s}$ applications, and is expressed as follows:

$$y_{v,e} = y_{v,s} - y_{v,pd} \tag{17}$$

The vestibular state error is given $x_{v,e} = x_{v,s} - x_{v,pd}$. The sensitive error LTI model can be expressed as:

$$\begin{aligned} \dot{x_{v,e}} &= A_v x_{v,e} + B_v u_s - B_v u_{pd}, \\ y_{v,e} &= C_v x_{v,e} + D_v u_s - D_v u_{pd} \end{aligned} \tag{18}$$

This problem can be formulated as a classical optimal control problem which seeks to minimize a cost function containing the quadratic form of the sensitive error and the control inputs while limiting the simulator movement. This cost function J based on the LQR, over [t0 t1], can be specified as:

$$\begin{aligned} J = E\{\int_{t_0}^{t_1}\big(y_{v,e}^T Q y_{v,e} + \xi_d^T R_d \xi_d + \\ + u_s^T R u_s\big) dt\}, \end{aligned} \tag{19}$$

where $y_{v,e}^T Q y_{v,e}$ denotes the perception error cost (perception validity), $\xi_d^T R_d \xi_d$ is the platform displacement cost, $u_s^T R u_s$ is the control input cost, E{} is the mean of the evaluation functions with respect to u_{pd} considered as filtered white noise as in [36], Q and R_d are positive semi definite matrices, and R is a positive definite matrix. To constrain the simulator motion, the $\xi_d^T R_d \xi_d$ part of the cost function must take the simulator's translational speed and displacement, and rotational speed. The principle of the MCA is to use the workspace efficiently and to bring the simulator back to its neutral position, for this we add the integral of the translational displacement. Therefore, we can define ξ_d as follows:

$$\begin{aligned} \xi_d &= \left(\iiint \ddot{x} dt^3 \iint \ddot{x} dt^2 \int \ddot{x} dt \theta_y\right)^T, \\ \dot{\xi_d} &= A_d \xi_d + B_d u_s, \end{aligned} \tag{20}$$

which are linked to the simulator input us through

$$A_d = \begin{pmatrix} 0 & 1 & 0 & 0 \\ 0 & 0 & 1 & 0 \\ 0 & 0 & 0 & 0 \\ 0 & 0 & 0 & 0 \end{pmatrix} \text{ and } B_d = \begin{pmatrix} 0 & 0 \\ 0 & 0 \\ 0 & 1 \\ 1 & 0 \end{pmatrix}$$

As recommended in [36], filtered white noise can be used as an input to the MCA in order to reproduce several scenario situations. This implies that an additional state space model needs to be incorporated to the one created earlier, whose states are the input. The predefined input upd can be considered as filtered white noises, and can be stated as follows:

$$\dot{x_n} = A_n x_n + B_n w, \tag{21}$$

where, x_n contains the filtered white noise states and w indicates white noise. A_n and B_n are given as:

$$A_n = \begin{pmatrix} -\gamma_1 & 0 \\ 0 & -\gamma_2 \end{pmatrix} \text{ and } B_n = \begin{pmatrix} \gamma_1 \\ \gamma_2 \end{pmatrix}, \tag{22}$$

where γ_1 and γ_2 are the cutoff frequencies.

The state space equations presented in (18), (20), and (21), can be combined to form the augmented state space equations and can be expressed as follows:

$$\begin{aligned} \dot{\chi} &= A\chi + Bu_s + Nw, \\ Y &= C\chi + Du_s, \end{aligned} \tag{23}$$

where $Y = \left(y_{v,e} \xi_d\right)^T$ is the desired output and $\chi = \left(x_{v,e} \xi_d x_n\right)^T \in \mathbb{R}^{12}$ contains the combined states. The combined system matrices $A \in \mathbb{R}^{12\times12}$, $B \in \mathbb{R}^{12\times2}$, $C \in \mathbb{R}^{6\times12}$, $D \in \mathbb{R}^{6\times2}$, and $N \in \mathbb{R}^{12\times1}$ are expressed as follows:

$$\begin{aligned} A &= \begin{pmatrix} A_v & 0_{(6\times4)} & -B_v \\ 0_{(4\times6)} & A_d & 0_{(4\times2)} \\ 0_{(2\times6)} & 0_{(2\times4)} & A_n \end{pmatrix}, \\ B &= \begin{pmatrix} B_v \\ B_d \\ 0_{(2\times2)} \end{pmatrix}, \\ C &= \begin{pmatrix} C_v & 0_{(4\times4)} & -D_v \\ 0_{(4\times6)} & I_4 & 0_{(4\times2)} \end{pmatrix}, \\ D &= \begin{pmatrix} D_v \\ 0_{(4\times2)} \end{pmatrix}, N = \begin{pmatrix} 0 \\ B_n \end{pmatrix}, \end{aligned} \tag{24}$$

with I_4 is the (4×4) identity matrix. In the design procedure of an optimal washout filter based on the LQR theory, several iterations are needed by changing the weighting matrices Q, R, and Rd for generating a suitable LQR-based optimal washout filter. The system equation and cost function can be transformed into the standard optimal control form, as follows:

$$\dot{\chi} = A_{tot}\chi + B\,u_{tot} + N\,w, \quad J_{tot} = E\{\int_{t_0}^{t_1}(\chi^T R_{tot1}\chi + u_{tot}^T R_{tot2} u_{tot})dt\}, \tag{25}$$

where $G = diag[Q, R_d]$, $R_{tot2} = R + D^T G D$, $R_1 = C^T G C$, $R_{12} = C^T G D, R_{tot1} = R_1 - R_{12} R_{tot2}^{-1} R_{12}^T$, $A_{tot} = A - B R_{tot2}^{-1} R_{12}^T$, $u_{tot} = u_s + R_{tot2}^{-1} R_{12}^T \chi$.

The cost function of (25) is minimized when

$$u_{tot} = -R_{tot}^{-1} B^T P \chi, \tag{26}$$

where P is the solution of the following algebraic Riccati equation:

$$R_{tot1} - P B R_{tot2}^{-1} B^T P + A_{tot}^T P + P A_{tot} = 0 \tag{27}$$

By specifying a matrix K, where $u_s = -K\chi$, we can get the following equation:

$$u_s = -(K_1\, K_2\, K_3)\begin{pmatrix} x_{v,e} \\ \xi_d \\ x_n \end{pmatrix}, \tag{28}$$

where $K = R_{tot2}^{-1}(B^T P + R_{12}^T)$ and $K_1 \in \mathbb{R}^{2\times 6}$, $K_2 \in \mathbb{R}^{2\times 4}$ $K_3 \in \mathbb{R}^{2\times 2}$. As $x_n = u_{pd}$, the states corresponding to x_n are eliminated. Thus, we get:

$$\begin{pmatrix} \dot{x_{v,e}} \\ \dot{\xi_d} \end{pmatrix} = \begin{pmatrix} A_v - B_v K_1 & -B_v K_2 \\ -B_d K_1 & A_d - B_d K_2 \end{pmatrix}\begin{pmatrix} \dot{x_{v,e}} \\ \dot{\xi_d} \end{pmatrix} + + \begin{pmatrix} -B_v(I_2 + K_3) \\ -B_d K_3 \end{pmatrix} u_{pd}$$

After developing the state space form of (18) and (29), the optimal filter that connects the predefined input and the simulator input can then be expressed as:

$$u_s(s) = W(s) u_{pd}(s), \tag{29}$$

where

$$W(s) = (K_1 K_2)\Gamma(s)\begin{pmatrix} B_v(I_2 + K_3) \\ B_d K_3 \end{pmatrix} - K_3, \tag{30}$$

where $\Gamma(s) = \begin{pmatrix} sI - A_v + B_v K_1 & B_v K_2 \\ B_d K_1 & sI - A_d + B_d K_2 \end{pmatrix}^{-1}$, and $W(s) \in \mathbb{R}^{2\times 2}$ is a matrix of the optimized transfer function based on the LQR theory that links the simulator motion input. In this method, the structure of the filter is part of the optimization process unlike other approaches where the structure of the filter is completely predefined (classic approach) or partially defined (adaptive approach). In addition, the predefined trajectory is no longer a simple deterministic signal but a band of signals (filtered white noise), the optimization certainly becomes less precise but in return, we are left with a filter usable in real-time.

The weighting matrices used in the LQR design were selected through an iterative manual tuning process to balance motion fidelity, control effort, and physical constraints of the simulator.

The final matrices used in the simulations are:

$$Q = diag([80, 80, 80]),$$
$$R = diag([0.058, 0.058]),$$
$$R_d = diag([0.1, 0.1, 0.1])$$

The predefined input was modeled as filtered white noise with cutoff frequencies:

$$\gamma_1 = 10, \gamma_2 = 10$$

The simulations were performed over a duration of T = 60 s with zero initial conditions.

4. Application: Skier Motion in $\mathbb{R}^2$ Space

Within the IBISC laboratory we have fully designed and developed from scratch a motion simulator called XY-6 DoF and is shown in Fig. 4.

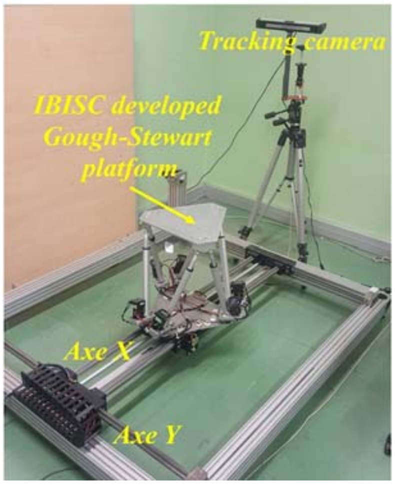

Fig. 4. XY-6 DoF simulator constructed at IBISC Laboratory.

The simulator consists of the well-known Gough-Stewart platform carried by two slider joints, X and Y, which form an XY-table, hence the name XY-6 DoF. To actuate the XY-6 DoF simulator we used the Nanotec PD4 servo motor due to its high performance and low weight. The translational movement of the sliders is obtained thanks to a mechanical rack wheel system. The translational movement of the hexapod legs is obtained thanks to the high-quality ball screw system, which transforms the rotational movement into translational movement.

In our work, we are interested in reproducing the ski scenario. The predefined scenario is defined and described in detail in the previous research work [15]. In order to find the simulator, input u_s using the optimal control, we need to introduce the simulator physical limits. We present in the following table the XY-6 DoF maximum of displacements, speeds and accelerations. In the following, we present the specific force restored by optimal approach in Fig. 5.

Table 1. XY-6 DoF motion interval.

D.o.F	Position	Max velocity	Max acceleration
X, Y	± 0.5 m	1.2 m/s	1.7 m/s²
X_p, Y_p, Z_p	± 0.1 m	0.8 m/s	1.1 m/s²
θ_x	± 15 deg	48.7 deg/s	71.6 deg/s²
θ_y	± 15 deg	48.7 deg/s	65.8 deg/s²
θ_z	± 15 deg	106 deg/s	154 deg/s²

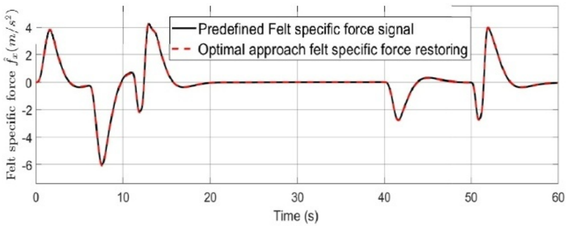

Fig. 5. Desired specific force from optimal algorithm.

The acceleration and specific force generated by the optimal filter show improved perceptual accuracy due to the coherence and proximity to the predefined trajectory. Fig. 6 shows the displacement, speed and acceleration of the hybrid simulator along the x-direction and Fig. 7 shows the tilt angle and tilt speed.

It is clear that the optimal approach can use the platform workspace more efficiently while respecting vestibular thresholds, can operate faster and be more precise compared to the classic and adaptive approach.

The simulator's displacement, speed, and acceleration resulting from the optimal approach have been determined according to the total capacity of the platform. Consequently, these movements exceed the capacity of either the table or the hexapod alone. A redundancy resolution must be developed to distribute the total simulator movement according to the capacity of each subsystem (hexapod and table).

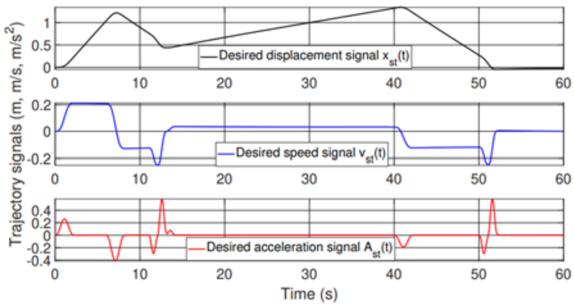

Fig. 6. Simulator trajectories along the x-direction.

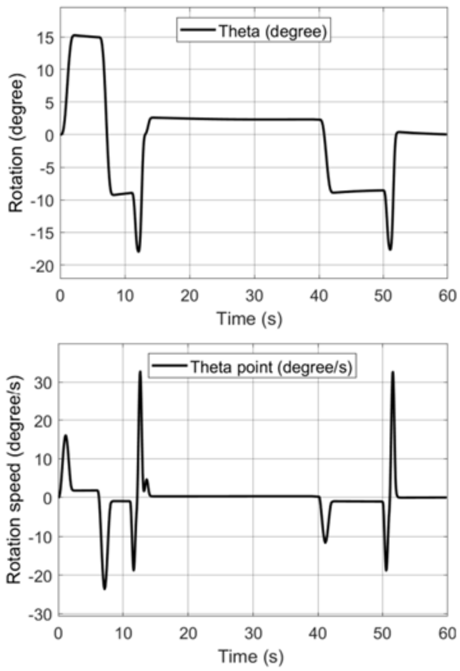

Fig. 7. Tilt angle and speed.

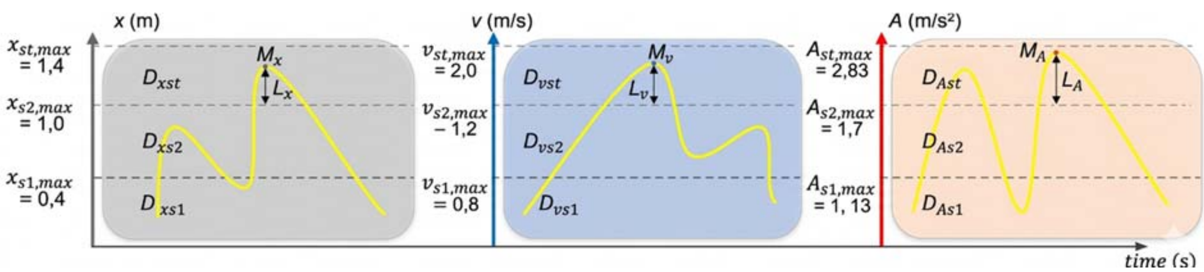

Fig. 8. Displacement, speed and acceleration workspaces.

First, we propose to use the hexapod mainly for tracking and performing the translation task once the XY table is inefficient. This means that the XY table will make the most significant translational move which is consistent with the purpose of introducing the XY table to the hexapod. Let us define *S*1 the first subsystem - hexapod, *S*2 the second subsystem – XY table and finally *St* the total system. Let us define the set $M = (M_x, M_v, M_a)$ where M_x, M_v, M_a denotes the maximum displacement, speed and acceleration of the predefined trajectory, respectively (obviously known for optimal approach). Fig 8 presents the displacement, speed and acceleration workspaces with its boundaries. The workspace boundaries are $x_{i,max}$, $v_{i,max}$, $A_{i,max}$ where $i = s1, s2, st$ for the first, the second subsystem and the total system. These boundaries are calculated from the real capacity of the platform motors using the direct kinematic model [24].

As described above, the most significant displacement will be mainly performed by the XY table. In the following, we present the proposed method to exploit the XY-6 DoF redundancy. First, if none of the M points M_x, M_v, M_A exceeds the capacity of the XY table, the XY table can perform the translational displacement alone. However, when one of the M points exceeds the capacity of the XY table, the hexapod must intervene and assist the XY table, as described below.

Let us take the case where one or more of the M points exceed the XY table capacity. Let us define L_x, L_v and L_A as the lack of displacement, speed and acceleration, respectively, that the XY table cannot perform. Moreover, let us define the dimensionless variables of L_x, L_v and L_A. Therefore

$$\begin{aligned} L_x &= M_x - x_{s2,max};\ L_{x_{dl}} = \frac{M_x - x_{s2,max}}{M_x} \\ L_v &= M_v - v_{s2,max};\ L_{v_{dl}} = \frac{M_v - v_{s2,max}}{M_v} \\ L_A &= M_A - A_{s2,max};\ L_{A_{dl}} = \frac{M_A - A_{s2,max}}{M_A} \end{aligned} \tag{31}$$

In addition to rotation movement, these translational trajectories lack should be performed by the hexapod. The total trajectory is designed by $x_{st}(t)$ which is equal to the trajectory performed by the XY table $x_{s2}(t)$ and the hexapod $x_{s1}(t)$. The two subsystems should perform the task in the same time conserving the same total desired trajectory, thus the trajectory of each subsystem can be composed as:

$$\begin{aligned} x_{s1}(t) &= \alpha x_{st}(t), \\ x_{s2}(t) &= (1-\alpha) x_{st}(t), \end{aligned} \tag{32}$$

where $\alpha \in$ R denotes the portion of the trajectory that should be performed by the hexapod, in other words the maximum lack of the XY table trajectory. Thus, α is the maximum of displacement, speed and acceleration lack.

$$\alpha = max\left(L_{x_{dl}}, L_{v_{dl}}, L_{A_{dl}}\right) \tag{33}$$

Since the hexapod model is non-linear thus the displacement, speed and acceleration capabilities are not similar. Therefore, we calculate the maximum displacement, speed and acceleration that can be performed by the hexapod by taking point M based on the 8-DoF simulator capacity. Therefore,

$$\begin{aligned} L_{x_{dl,max}} &= 28.5\ \%, \\ L_{v_{dl,max}} &= 40\ \%, L_{A_{dl,max}} = 40\ \% \end{aligned} \tag{34}$$

We can see that even if the hexapod has greater capacities in speed and acceleration than in displacement but it should still be limited by the displacement. Therefore α will be limited by the minimum of the maximum lack which is $L_{xdl,max}$. Thus

$$\alpha = min\left[max\left(L_{x_{dl}}, L_{v_{dl}}, L_{A_{dl}}\right), L_{x_{dl,max}}\right] \tag{35}$$

We summarize the proposed algorithm.

Algorithm 1. Redundancy Exploitation Algorithm

```
Initialization;
    Apply Optimal MCA;
Mx= max(xst(t));(Total desired displacement);
Mv= max(vst(t)); (Total desired speed);
MA=max(Ast(t));(Total desired acceleration);

X-Table Limits;
    xs2max = 1;  (Displacement limit);
    vs2max = 12; (Speed limit);
    As2max = 1.7;(Acceleration limit);

If((Mx>xs2max)OR(Mv>vs2max)OR(MA>As2max))
then
    Lx,dl=(Mx-xs2max)/Mx;(Displacement lack);
    Lv,dl=(Mv-vs2max)/Mv; (Speed lack);
    LA,dl=(MA-As2max)/MA;(Acceleration lack);

    Lm = max(Lx,dl, Lv,dl, LA,dl);  (Maximum
dimensionless lack);

    α = min(Lm, 0.285);
Else
    α = 0;
End If

Result;
    xs1(t) = α * xst(t);
    vs1(t) = α * vst(t);
    As1(t) = α * Ast(t);

    xs2(t) = (1 - α) * xst(t);
    vs2(t) = (1 - α) * vst(t);
    As2(t) = (1 - α) * Ast(t);
```

Let us apply the redundancy resolution to the trajectory result from the optimal MCA approach (Fig. 6). The maximum displacement, speed and acceleration are M: (M_x = 1.276 m, M_v = 0.313 m/s, M_A = 0.798 m/s^2). M_x is greater than the table displacement workspace which requires the use of the hexapod. Thus, we calculate the amount of the assistance provided by the hexapod L_x = 0.276 m, L_v = 0 m/s, L_A = 0 m/s^2. Consequently, compared to our constraints, for this specific task, the hexapod will carry $\alpha = L_{xdl}$ = 0.216 of the total trajectories which corresponds to 21.6 % and the X-table will carry the 78.4 %. Therefore, the total desired trajectories are clearly distinguished in hexapod and X-table trajectories shown in Fig. 9 and Fig. 10.

Fig. 9 and Fig. 10 show that the entire trajectory can be split into two trajectories achievable by each subsystem while maintaining the same human sensation. In summary, we have designed an optimal approach that considers human sensation via the vestibular system model and the physical limits of our platform XY-6 DoF. Using the optimal approach, we may deduce the upper platform behavior (at the human vestibular level) that corresponds to the total system trajectories. We therefore proposed the redundancy exploitation algorithm to generate the trajectories of each subsystem, hexapod and table, from the total trajectories.

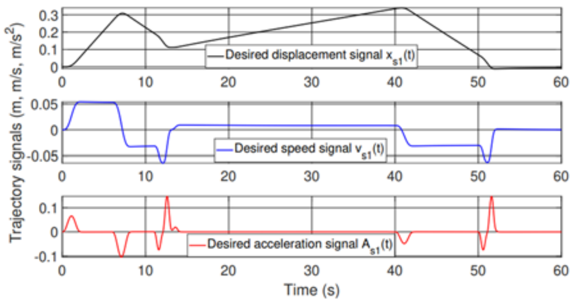

Fig. 9. Desired Hexapod trajectories.

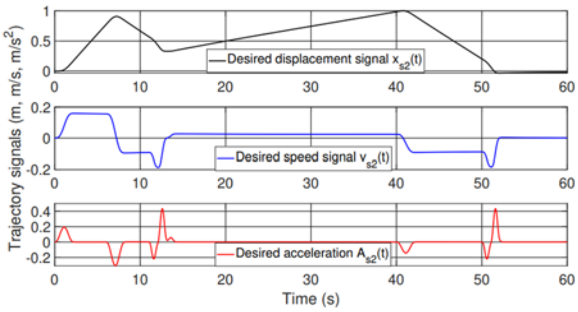

Fig. 10. Desired X-Table trajectories.

Motion fidelity can be defined as the degree to which the motion cues match those of the actual skier. Motion fidelity is affected by several factors, in particular the motion platform hardware and the MCA algorithm. Since motion tracking is subjective, motion fidelity is usually measured subjectively. Subjective assessment is performed using scales or questionnaires that pilots/skiers are asked to complete. Subjective assessment is the natural way to validate MCA and is fairly ”easy” to perform. However, it has several drawbacks. First, there can be large differences between pilots/skiers, even with the same simulator and under the same conditions. In addition, the operator’s responses may depend on the timing of the assessment, the particular sequence or order of the tests, the individual’s personal preferences or even the nature of the assessment. In fact, the same person may provide different evaluations on different days, for the same simulator and under the same conditions. Therefore, subjective evaluation cannot provide repeatability nor reliability.

As our XY- 6 DoF platform is a prototype for the validation of algorithms and architecture and it is not possible to integrate a human being. To objectively evaluate the motion fidelity, we introduce a performance indicator (PI). This metric quantifies the similarity between the simulated motion cues and the predefined (reference) motion cues. This PI takes into account the scale of the generated movements with respect to the original scale (amplitude distortion) and the time-delay (phase distortion) produced by the motion platform’s inertial nature and by the effects of frequency filtering.

$$PI = 100\left(1 - \frac{\| F_{sim}(t) - F_{pd}(t) \|_2}{\| F_{pd}(t) \|_2}\right), \tag{36}$$

where $F_{sim}(t)$ is the simulated specific force generated by the motion platform, $F_{pd}(t)$ is the predefined (reference) specific force corresponding to the real skier motion, $\|.\|_2$ denotes the Euclidean (L2) norm computed over the simulation time interval.

The PI is computed over the entire simulation duration using discrete-time samples of the signals. This formulation captures both amplitude discrepancies and temporal misalignment (phase distortion) between the simulated and reference signals.

The value of PI ranges between 0 and 1, where, PI = 1 indicates a perfect match between simulated and real motion cues and lower values indicate increasing deviation and reduced motion fidelity. Using this metric, the proposed optimal approach achieves a PI value of 97 % representing the highest performance reported to date. Compared to previously published results [2, 15], where classical methods achieved PI values of 63.25 % and 77.57 %, adaptive approaches reached up to 95 %, and PSO-based optimization attained 96.66 %, the proposed approach provides a clear improvement. This confirms the effectiveness and superiority of the proposed method, establishing it as a state-of-the-art solution for MCA optimization. The results show the effectiveness of the proposed optimal washout filter on many levels: reduce the human sensation error, maximize the shape following factor and use the entire XY-6 DoF platform workspace availability.

5. Conclusions

In this article, we addressed the limitations of existing Motion Cueing Algorithms (MCAs), which often neglect both the human vestibular perception and the efficient use of the simulator workspace. To overcome these challenges, we propose a multi-objective optimal washout filter based on Linear Quadratic Regulator (LQR) theory that explicitly incorporates a mathematical model of the human vestibular system.

The proposed approach minimizes perceptual error while respecting the physical constraints of the motion platform, leading to a significant improvement in motion fidelity. Simulation results demonstrated that the method achieves up to 97 % recovery of human perception, highlighting its effectiveness compared to classical and adaptive approaches.

Furthermore, we introduced a novel redundancy resolution strategy for an 8-DoF hybrid simulator, enabling an optimal distribution of motion between the hexapod and the XY-table. This approach ensures efficient workspace utilization while preserving realistic motion cues, thereby enhancing the overall simulation experience.

Despite these promising results, the current study is limited to simulation-based validation. Future work will focus on integrating a real-time tracking controller that accounts for the coupled dynamics of the vestibular system and the hybrid platform. In addition, experimental validation involving human subjects or humanoid robotic systems will be conducted to further assess the realism and effectiveness of the proposed method.

Overall, this work contributes to the development of more accurate and human-centered motion simulation systems, with potential applications in rehabilitation, training, and immersive virtual environments.

Availability of Data and Materials

Data sharing is not applicable to this article as no datasets were generated or analyzed during the study.

References

[1]. S. Seher, K. Abedi, K. Fatima, S. Badiwala, et al., VR applications and vision-based recognition techniques for sign language: A survey, in *Proceedings of the 16th IEEE International Conference on Computational Intelligence and Communication Networks (CICN)*, 2024, pp. 1527-1533.

[2]. T. Houda, L. Beji, A. Amouri, M. Mallem, Dynamic behavior of an interactive XY-6 DoF simulator for people with reduced mobility, in *Proceedings of the IEEE Conference on Control Technology and Applications (CCTA)*, 2020, pp. 522-527.

[3]. S. de Groot, J. de Winter, M. Mulder, P. A. Wieringa, Nonvestibular motion cueing in a fixed-base driving simulator: Effects on driver braking and cornering performance, *Presence: Teleoperators and Virtual Environments*, Vol. 20, Issue 2, 2011, pp. 117-142.

[4]. R. A. Wynne, V. Beanland, P. M. Salmon, Systematic review of driving simulator validation studies, *Safety Science*, Vol. 117, 2019, pp. 138-151.

[5]. J. G. Allen, P. MacNaughton, J. G. Cedeño-Laurent, X. Cao, et al., Airplane pilot flight performance on 21 maneuvers in a flight simulator under varying carbon dioxide concentrations, *Journal of Exposure Science & Environmental Epidemiology*, Vol. 29, Issue 4, 2019, pp. 457-468.

[6]. Y. Wu, K. Kihara, Y. Takeda, T. Sato, et al., Effects of scheduled manual driving on drowsiness and response to take over request: A simulator study towards understanding drivers in automated driving, *Accident Analysis and Prevention*, Vol. 124, 2019, pp. 202-209.

[7]. E. Perera, G. Villoing, S. Ruffié, Devenir pilote handiski: Valoriser la lenteur pour sécuriser l'expérience de glisse handisportive en station de ski, *Nature & Récréation*, Issue 7, 2019, pp. 22-30 (in French).

[8]. T. Houda, A. Beghdadi, L. Beji, A. Amouri, Multi-complex robot interaction with homothetic human feedback in a virtual environment, *Sensors & Transducers*, Vol. 260, Issue 2, 2023, pp. 15-24.

[9]. N. J. I. Garrett, M. C. Best, Driving simulator motion cueing algorithms - a survey of the state of the art, *Proceedings of the Institution of Mechanical Engineers, Part D: Journal of Automobile Engineering*, Vol. 224, Issue 4, 2010, pp. 537-550.

[10]. T. Houda, A. Amouri, A. Beghdadi, L. Beji, Multi-robot interaction with mixed reality for enhanced perception, in Smart Applications and Data Analysis (M. Hamlich, F. Dornaika, C. Ordonez, L. Bellatreche, et al., Eds.), *Springer*, Cham, 2024, pp. 219-232.

[11]. D. Petrovic, R. Mijailovic, D. Pesic, How to improve the inclusion of drivers with disabilities: Measures to enhance accessibility, mobility, and road safety, *Journal of Transportation Engineering, Part A: Systems*, Vol. 148, Issue 3, 2022, 04021122.

[12]. J. Ku, D. P. Jang, H. B. Ahn, J. Lee, et al., The development and clinical trial of a driving simulator for the handicapped, *Studies in Health Technology and Informatics*, Vol. 85, 2002, pp. 240-246.

[13]. R. A. Telban, F. M. Cardullo, Motion cueing algorithm development: A human-centered approach, Technical Report NASA/CR-2005-213747, *National Aeronautics and Space Administration*, 2005.

[14]. M. A. Nahon, L. D. Reid, Simulator motion-drive algorithms - A designer's perspective, *Journal of Guidance, Control, and Dynamics*, Vol. 13, Issue 2, 1990, pp. 356-362.

[15]. T. Houda, L. Beji, A. Amouri, M. Mallem, Handiski simulator performance under PSO-based washout and control parameters optimization, *Nonlinear Dynamics*, Vol. 108, Issue 3, 2022, pp. 2161-2182.

[16]. H. Şahin, V. H. Dang, E. Sayar, A. Yegenoglu, et al., Fuzzy logic theory-based adaptive reward shaping for robust reinforcement learning (FARS), *arXiv*, 2026, arXiv:2604.15772.

[17]. L. D. Reid, M. Nahon, Flight simulation motion-base drive algorithms: Part 1. Developing and testing equations, Technical Report UTIAS 296, *University of Toronto Institute for Aerospace Studies*, 1985.

[18]. M. R. C. Qazani, H. Asadi, T. Bellmann, S. Pedrammehr, et al., A new fuzzy logic based adaptive motion cueing algorithm using parallel simulation-based motion platform, in *Proceedings of the IEEE International Conference on Fuzzy Systems (FUZZ-IEEE)*, 2020, pp. 1-8.

[19]. S. Nahavandi, Industry 5.0 – A human-centric solution, *Sustainability*, Vol. 11, Issue 16, 2019, 4371.

[20]. A. Gharib, M. Goharimanesh, A. Koochi, M. R. Gharib, Designing an evolutionary optimal washout filter based on genetic algorithm, *Aviation*, Vol. 26, Issue 4, 2022, pp. 193-201.

[21]. A. R. Naseri, P. R. Grant, Difference threshold: Measurement and modeling, in Proceedings of the *International Conference on Motion Perception and Simulation*, 2011.

[22]. T. Houda, A. Beghdadi, L. Beji, A. Amouri, Complex multi-robot hybrid platform for augmented virtual skiing immersion, in *Proceedings of the 3rd IFSA Winter Conference on Automation, Robotics & Communications for Industry 4.0/5.0 (ARCI)*, 2023, pp. 95-99.

[23]. M. Tanaka, F. Matsuno, Modeling and control of head raising snake robots by using kinematic redundancy, *Journal of Intelligent & Robotic Systems*, Vol. 75, Issue 1, 2014, pp. 53-69.

[24]. T. Houda, A. Amouri, L. Beji, M. Mallem, Dynamic parameters optimization and identification of a parallel robot, in Multibody Dynamics 2019 (A. Kecskeméthy, F. Geu Flores, Eds.), *Springer*, Cham, 2020, pp. 285-292.

[25]. A. L. Orekhov, N. Simaan, Directional stiffness modulation of parallel robots with kinematic redundancy and variable stiffness joints, *Journal of Mechanisms and Robotics*, Vol. 11, Issue 5, 2019, 051001.

[26]. S.-H. Cha, T. A. Lasky, S. A. Velinsky, Singularity avoidance for the 3-RRR mechanism using kinematic redundancy, in *Proceedings of the IEEE International Conference on Robotics and Automation (ICRA)*, 2007, pp. 1195-1200.

[27]. J. Baillieul, J. M. Hollerbach, R. W. Brockett, Programming and control of kinematically redundant manipulators, in *Proceedings of the 23rd IEEE Conference on Decision and Control (CDC)*, 1984, pp. 768-774.

[28]. T. Houda, L. Beji, A. Amouri, Multi-objective LQR-based optimization of motion cueing for redundant ski simulator, in *Proceedings of the 6th IFSA Winter Conference on Automation, Robotics & Communications for Industry 4.0/5.0/6.0 (ARCI)*, 2026, pp. 1-13.

[29]. W. E. Omer, K. Abdulhadi, Physiology and diagnostic tests of the vestibular system, in Textbook of Clinical Otolaryngology (A. Al-Mujaddidi, Ed.), *Springer*, Cham, 2020, pp. 169-183.

[30]. F.-O. Bohoua-Nassé, Compréhension et modélisation du comportement conducteur et de sa perception, Master's Thesis, *École des Mines de Paris*, Paris, 2004 (in French).

[31]. L. R. Young, J. L. Meiry, A revised dynamic otolith model, *Aerospace Medicine*, Vol. 39, Issue 6, 1968, pp. 606-608.

[32]. J. Laurens, D. E. Angelaki, The functional significance of velocity storage and its dependence on gravity, *Experimental Brain Research*, Vol. 235, Issue 12, 2017, pp. 3507-3521.

[33]. J. A. Houck, R. J. Telban, F. M. Cardullo, Motion cueing algorithm development: Human-centered linear and nonlinear approaches, Technical Report NASA/TP-2005-213745, *National Aeronautics and Space Administration*, 2005.

[34]. A. Berthoz, I. Viaud-Delmon, Multisensory integration in spatial orientation, *Current Opinion in Neurobiology*, Vol. 9, Issue 6, 1999, pp. 708-712.

[35]. G. L. Zacharias, Motion cue models for pilot-vehicle analysis, Technical Report AMRL-TR-78-2, *Defense Technical Information Center*, 1978.

[36]. S.-H. Chen, L.-C. Fu, An optimal washout filter design with fuzzy compensation for a motion platform, *IFAC Proceedings Volumes*, Vol. 44, Issue 1, 2011, pp. 8433-8438.